

# Drag and lift forces on interface-contaminated bubbles spinning in a rotating flow

MARIE RASTELLO†, JEAN-LOUIS MARIÉ,  
NATHALIE GROSJEAN AND MICHEL LANCE

Laboratoire de Mécanique des Fluides et d'Acoustique, Ecole Centrale de Lyon-CNRS-Université  
Claude Bernard Lyon 1-INSA Lyon, 36 Avenue Guy de Collongue, 69134 Ecully cedex, France

(Received 31 January 2008 and in revised form 24 November 2008)

The equilibrium position of a spherical air bubble in a solid body rotating flow around a horizontal axis is investigated experimentally. The flow without bubbles is checked to be solid body rotating. The area of influence of the bubble is characterized to determine for each bubble whether the incoming flow is perturbed or not. The demineralized water used is shown to be contaminated, and spinning of the bubble's interface is observed and measured. From the measurement of the bubble's equilibrium position, drag and lift coefficients are determined. They appear to be dependent on two dimensionless numbers.  $Eo$  the Eötvös number and  $R_\omega$  the rotational Reynolds number (or Taylor number  $Ta$ ) can be varied independently by changing the control parameters, and for that reason are the convenient choice for experiments. ( $Re$ ,  $Ro$ ) with  $Ro$  the Rossby number is an equivalent choice generally adopted in the literature for numerical simulations, and  $Re$  denotes the Reynolds number. When using this second representation, the  $Ro$  number appears to be an indicator of the influence on the force coefficients of the shear, of the curvature of the streamlines of the flow and of the bubble's spinning. The bubble's spinning effect on the lift force is far from trivial. Its contribution explains the important gap between lift values for a bubble (not spinning) in a clean fluid and for a bubble (spinning) in a contaminated fluid as present.

---

## 1. Introduction

In many industrial processes such as the oil industry or chemical engineering it is essential to be able to predict particles or bubbles' trajectories, and to do so it is necessary to know the applied forces on the inclusions. Significant progress has been made and the forces on an isolated bubble have been determined in several flow situations. For instance, the case of a bubble in a linear shear flow is now well documented. Legendre & Magnaudet (1998) carried out a detailed numerical study of the case of a spherical fixed bubble in a linear shear flow for a large range of Reynolds numbers. Lift and drag forces were derived. The low-Reynolds-number case was studied analytically by Legendre & Magnaudet (1997) extending Saffman (1965)'s results for a solid sphere. Auton (1987) investigated the other limit, that of inviscid flows, and obtained an analytical expression of the lift force for a spherical body. The lift coefficient was found to be 0.5 for high Reynolds numbers. Unfortunately many configurations remain in which the bubbles' behaviour and applied forces are

† Email address for correspondence: marie.rastello@ec-lyon.fr

not fully determined. The case of one bubble in a solid body rotating flow (*SBRH*) is one of them. This simple configuration is of interest in itself and also in that it does not include any strain effect, contrary to a linear shear flow. Hence, it is meaningful for whosoever attempts to derive a more general expression of the forces acting on a bubble in a complex flow, by decomposing this flow into a superposition of simpler ones. This kind of decomposition has been tackled in the case of simple shear flow by Magnaudet & Legendre (1998) and appears to be promising. Studies concerning a single bubble in an *SBRH* are not many. Naciri (1992) studied experimentally the forces on a bubble in a flow in solid body rotation around a horizontal axis. He worked with a slightly deformed bubble, in a fluid which is a mixture of water and glycerine, for Reynolds numbers ranging from 10 to 100. He found that the bubble reaches an equilibrium position from which he measured lift coefficients of the order of 0.2–0.3. Magnaudet & Legendre (1998) numerically computed the forces on a clean spherical bubble kept fixed in this type of flow. They fit their lift data for  $Re > 50$  with a function of  $Re$  and showed that the lift coefficient recovers the 0.5 inviscid value obtained by Auton (1987) in a weak linear shear, but for Reynolds numbers larger than a thousand. Compared with a pure shear, they concluded that the contribution of the viscous effects vanish less rapidly in this type of non-symmetrical flow. More recently, van Nierop *et al.* (2007) revisited Naciri (1992)'s experiment. They worked with the same fluids, but focused on spherical bubbles over a wide  $Re$  range. One of the remarkable results is a change of sign of the lift coefficient that becomes negative when  $Re < 5$ . Juaneda & Colin (2007) turned their attention to low Reynolds bubbles ( $Re \leq 10$ ) in a Couette flow. The effect of the wall of the cylinder on the forces has been studied. Other studies exist that deal with different kinds of rotating flows and/or moving objects in them. As an example, Sridhar & Katz (1995) studied the behaviour of microscopic bubbles entrained by a vortex, Candelier, Angilella & Souhar (2004) studied rising bubbles in a flow rotating around a vertical axis with low Reynolds numbers. In the domain of solid particles, Bagchi & Balachandar (2002*b*) looked at the forces applied to a rigid sphere in an *SBRH* and compared the results with those they obtained for a linear shear flow. The authors mention that their results agree qualitatively with the data of Sridhar & Katz (1995) but are markedly different from those found by Legendre & Magnaudet (1998) and Magnaudet & Legendre (1998) for clean bubbles. As a rule, there are significant discrepancies in the order of magnitude of the lift coefficients reported in the literature. These discrepancies mainly arise from differences in the boundary conditions at the interface (slip or non-slip condition) and whether the bubble is free (experiments) or fixed (most of simulations).

The present study deals with bubbles at equilibrium in an *SBRH* around a horizontal axis. As in Naciri (1992) and van Nierop *et al.* (2007), the purpose is to determine the forces applied to a free bubble from measurement of the equilibrium position. Compared to these two previous experiments, we work exclusively in demineralized water over an intermediate range of Reynolds number ( $4 < Re \leq 280$ ) with bubbles that remain spherical. We are concerned with the case of bubbles with a contaminated interface, i.e. the situation commonly encountered over this range of diameters in water applications. No extreme precaution was therefore taken to keep this water perfectly pure, as is the case in Duineveld (1995) or de Vries, Biesheuvel & van Wijngaarden (2002). We find that, depending on where the bubble is stabilizing in the tank, the bubble's presence can highly perturb the solid body rotation flow. These critical equilibrium positions must be avoided for the determination of the forces. We also show by imaging that spinning of the bubble's interface occurs. This induces an additional lift component. We give evidence that the interface of our bubble is

contaminated, so that the bubble no longer behaves like a clean bubble experiencing a shear-free condition at its interface. Subsequently, the bubble is set in rotation by the basic flow and reaches an equilibrium state of spinning. The next section of this paper provides the governing equations for this study and dimensionless numbers to describe the bubble's behaviour. The experimental device is then presented and bubble's behaviour and flow characteristics are studied. Finally, the measured drag and lift forces are reported and discussed.

## 2. Force balance, dimensionless numbers

A bubble rising freely under buoyancy force in a stagnant viscous liquid reaches a terminal velocity depending on its size and the liquid's properties. The well-known diagram of Clift, Grace & Weber (1978) makes it possible to classify the different regimes of rise as a function of a bubble Reynolds number, an Eötvös or Bond number and a property number (or Morton number), with a relation of the form

$$Re = F(Eo, M). \quad (2.1)$$

Experimentally, it is possible to keep the bubble fixed with respect to the laboratory frame when it is injected into a liquid moving uniformly downwards, with a velocity which is exactly opposite to the bubble's terminal velocity (see, for example, Alves, Orvalho & Vasconcelos 2005). A similar but slightly more complex situation occurs when the bubble is injected into a liquid in solid rotation around a horizontal axis. As a matter of fact, the bubble will move into the liquid to reach a location where the gravity force is balanced by the drag force exerted by the fluid on the bubble and by the additional transverse forces arising from the non-uniformity of the flow. As a result, the equilibrium position of the bubble, which will be discussed in more detail later on, is not in general in the horizontal plane of symmetry passing through the axis of rotation. The consequence is that the observable unknown is not only the intensity of the relative velocity of the bubble with respect to the liquid (noted  $U_R$ ), but also its orientation. Of course, the most convenient reference is the direction of gravity, so that a possible choice to quantify the unknown velocity vector  $\mathbf{U}_R$  is its intensity  $U_R$  and its projection on the gravity vector  $\mathbf{g}$ , or which is equivalent, the cosine  $\cos\theta_e = \mathbf{U}_R \cdot \mathbf{g} / (U_R g)$ . In the present experiment, the rotation is uniform and characterized only by the speed of rotation  $\omega$ . Therefore, the control parameters are the gravity vector  $\mathbf{g}$ , the liquid kinematic viscosity  $\nu$ , the liquid density  $\rho_l$ , the surface tension  $\sigma$ , the density difference  $\Delta\rho = \rho_l - \rho_g \approx \rho_l$ , the bubble equivalent diameter  $d$  and the rotation speed  $\omega$ . Here, the gas viscosity and the gradient of surface tension due to possible interface contamination are not included. Gas density is neglected because  $\rho_g \ll \rho_l$ . A straightforward dimensional analysis shows that the equivalent of Clift *et al.* (1978)'s representation for the rotating motion is

$$Re = F(Eo, M, R_\omega), \quad (2.2)$$

$$\theta_e = G(Eo, M, R_\omega), \quad (2.3)$$

where  $Re$  is the bubble's Reynolds number  $Re = U_R d / \nu$ ,  $Eo$  is the Eötvös number  $Eo = g \Delta\rho d^2 / \sigma$ ,  $M$  is the so-called Morton number  $M = g \rho^2 \nu^4 \Delta\rho / \sigma^3$  and  $R_\omega$  a rotational Reynolds number  $R_\omega = \omega d^2 / \nu$ .

For a spherical bubble, moving relative to the fluid at a moderate to large Reynolds number, the dynamical equation commonly adopted to describe bubble

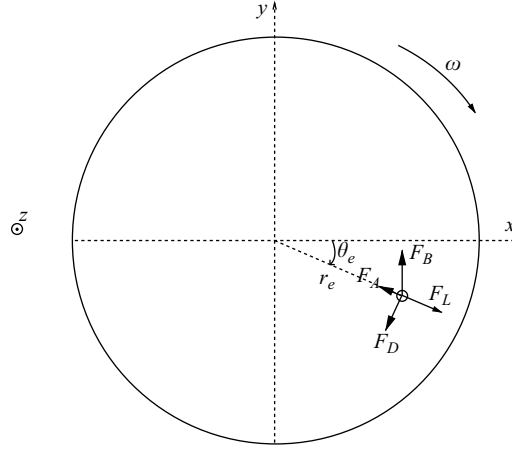


FIGURE 1. The forces applied to a bubble at equilibrium at moderate to high Reynolds numbers.  $F_B$  is the buoyancy force,  $F_D$  the drag force,  $F_L$  the lift force.  $F_A$  takes into account the added mass force and pressure gradient effects. In the present sketch, the angular velocity  $\omega$  and equilibrium angle  $\theta_e$  are negative.

motion is (Magnaudet & Eames 2000)

$$\rho_l V_b C_A \frac{d\mathbf{v}}{dt} = -\rho_l V_b \mathbf{g} + \rho_l V_b (C_A + 1) \frac{D\mathbf{U}}{Dt} t + \rho_l V_b C_L (\mathbf{U} - \mathbf{v}) \times (\nabla \times \mathbf{U}) + \frac{1}{2} \rho_l C_D A_b |\mathbf{U} - \mathbf{v}| (\mathbf{U} - \mathbf{v}), \quad (2.4)$$

where  $\rho_l$  is the liquid density,  $V_b$  the volume of the bubble,  $A_b$  its projected area,  $\mathbf{v}$  bubble's velocity,  $\mathbf{g}$  gravity acceleration and  $\mathbf{U}$  the velocity of the undisturbed ambient flow taken at the centre of the bubble. The forces considered in this equation are respectively buoyancy  $F_B$ , added mass and pressure gradient  $F_A$ , lift  $F_L$  and drag  $F_D$ .  $C_A$  is the added mass coefficient. Its value is 0.5 for spherical bubbles (Magnaudet & Eames 2000). It depends on the aspect ratio for ellipsoidal ones (Lamb 1934)

$$C_A = \frac{\gamma_0}{2 - \gamma_0} \text{ with } \gamma_0 = \frac{2}{e^2} \left( 1 - \sqrt{1 - e^2} \frac{a \sin(e)}{e} \right) \text{ and } e = \frac{\sqrt{\chi^2 - 1}}{\chi} \quad (2.5)$$

with  $\chi$  the ratio of the major axis to the minor axis of the bubble.  $C_L$  is the lift coefficient and  $C_D$  the drag coefficient. In the present experiment the undisturbed flow field  $\mathbf{U}$  is an *SBRH* at constant angular velocity  $\omega$  around a horizontal axis. In this case all the forces balance when the flow is stationary and the bubble comes to an equilibrium position (see figure 1) where  $\mathbf{v} = 0$ . With  $\mathbf{U} = \omega r_e \mathbf{e}_\theta$ , (2.4) becomes

$$C_L = \frac{1}{2} \left( 1 + C_A - \frac{g \sin \theta_e}{r_e \omega^2} \right) \quad (2.6)$$

and

$$C_D = \frac{4}{3} \frac{g d \cos \theta_e}{r_e^2 \omega^2}, \quad (2.7)$$

where  $(r_e, \theta_e)$  are the polar coordinates  $(r, \theta)$  of the centre of the bubble at equilibrium and  $d$  the equivalent diameter of the bubble. Thus, if one measures  $r_e$  and  $\theta_e$ ,  $d$  and  $\omega$ , and calculates  $C_A$  from the aspect ratio  $\chi$ , one can calculate the values of  $C_L$  and  $C_D$ . It is easily verified that the elimination of  $U_R$  and  $\theta_e$  between (2.1), (2.2), (2.6)



FIGURE 2. Picture of the experimental device showing the tank. In the front is the high-speed camera. At the back the toothed belt can be seen.

and (2.7) yields

$$C_L = C_L(Eo, M, R_\omega)$$

and

$$C_D = C_D(Eo, M, R_\omega).$$

This representation proves to be the most convenient for running the experiment since, for given fluid properties (or  $M = Cst$ ), the Eötvös number and the rotational Reynolds number can be varied independently by changing  $\omega$  and  $d$ . Recent works in the literature (van Nierop *et al.* 2007) use another equivalent representation based on the choice of the distance  $r_e$  as a length scale. If one keeps the Morton number constant, this amounts to replacing  $Eo$  and  $R_\omega$  by the bubble Reynolds number and the dimensionless shear number  $S$  (e.g.)

$$C_L = C_L(S, Re)$$

and

$$C_D = C_D(S, Re)$$

with  $S = \omega d / U_R = d / r_e$ . This choice might not be the most convenient, since  $S$  and  $Re$  are not control parameters in the experiments. However, they turn out to be control parameters for the numerical simulations and so are interesting for easier comparisons with experimental results, like in van Nierop *et al.* (2007). In order to comply with the representation adopted in the literature, the results are here discussed as a function of  $Re$  and  $Ro = U_R / \omega d = r_e / d$  the Rossby number, which, for the solid body rotation investigated here is simply  $S^{-1}$ .

### 3. Experimental features

#### 3.1. Experimental setup and procedure

The device is a cylindrical tank ( $\varnothing = 10$  cm,  $L = 10$  cm) rotating around its axis. The axis is horizontal. The tank is made of Plexiglas and is mounted in a cylindrical counterbore and the contact is made using ball bearings (see figure 2). A motor is coupled to the tank, at the back, using a toothed belt. For this set of experiments, the range of rotation rates for the tank is from around  $3 \text{ rad s}^{-1}$  to around  $20 \text{ rad s}^{-1}$ . The front face of the tank is removable for cleaning. Three aligned holes have been made on the side of the cylinder. They are closed with stoppers. They are used to fill in the tank

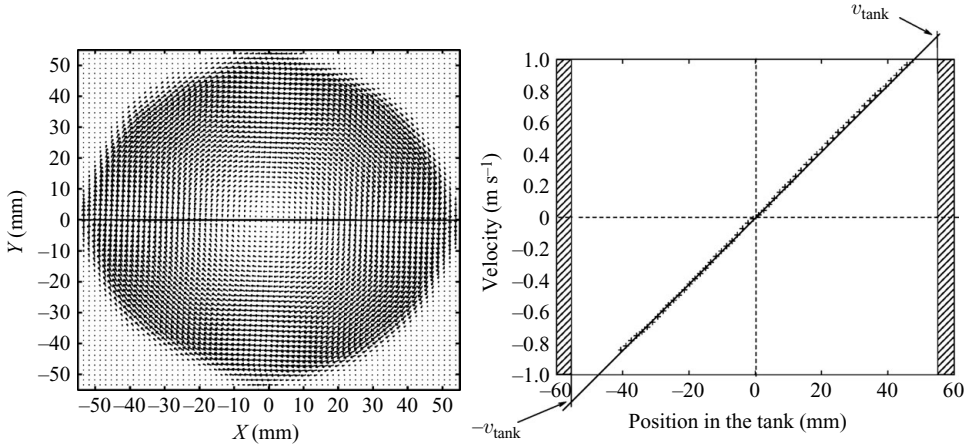


FIGURE 3. Example of velocity vectors obtained by PIV (Left). (Right) Velocity profile obtained, cutting the velocity field along the horizontal black line. The velocity profile is linear. The fluid's velocity towards the edges of the tank is equal to the velocity of the tank. The flow is a solid body rotation.

with water and to inject the bubble. The experimental procedure is the following. The temperature ( $T$ ) of the demineralized water contained in the tank is measured using a thermometer. A bubble is then injected into the tank. After that, the tank is set in rotation. A few minutes are allowed to pass so that the fluid is in *SBRH* and the bubble stabilizes at equilibrium. Then measurements are carried out (see § 3.3). Typical values are  $T \in [21^\circ\text{C}, 27^\circ\text{C}]$ ,  $d \in [0.24 \text{ mm}, 1.6 \text{ mm}]$ ,  $\chi \in [1, 1.15]$ ,  $Re \in [4, 280]$ ,  $Ro \in [5, 35]$ ,  $EO \in [8 \times 10^{-3}, 0.35]$ ,  $R_\omega \in [0.35, 40]$ ,  $C_A \in [0.5, 0.6]$ . Temperature values are used to compute the water viscosity for each run.

### 3.2. Flow characterization

The first stage is to study the flow without bubbles to check that it is an *SBRH*. Velocity profiles were measured using standard PIV (frame rate = 15 frames  $\text{s}^{-1}$ ) and small hollow glass spheres ( $d = 10 \mu\text{m}$ ) as seeding particles. The laser sheet was perpendicular to the flow's axis of rotation. It was found that the velocity profiles were linear over the whole section of the tank for every rotation rate (see figure 3) and well matched with the velocity of the tank at the wall. The second stage of the study is to determine the area perturbed by the bubble's presence. The goal is to check whether the incoming flow on the bubble is still an *SBRH* or is perturbed. The bubble's wake and perturbed area were visualized using both high-speed PIV (frame rate = 900 frames  $\text{s}^{-1}$ ) and long-time exposure pictures. For both, small fluorescent polyamid seeding particles ( $d = 10 \mu\text{m}$ ) were used, and the laser sheet was again perpendicular to the rotation axis. High-speed PIV enabled us to have access to the perturbed velocity fields. Indeed, by simply translating the laser sheet we measured, during the same run, the *SBRH* velocity fields in a plane containing the bubble and in a plane not affected by the bubble and located far from its equilibrium position. By subtracting these two *SBRH* velocity fields with and without the bubble it was then possible to extract only the flow perturbation caused by the presence of the bubble. For small bubbles, with  $Re \lesssim 60\text{--}70$ , the wake behind the bubble is very small. It vanishes very rapidly. The incoming flow on the bubble has no reminiscence of it whatever the position of the bubble in the tank (see figure 4). For larger bubbles ( $60\text{--}70 \lesssim Re$ ) the bubble's wake extends farther downstream from the bubble equilibrium position and

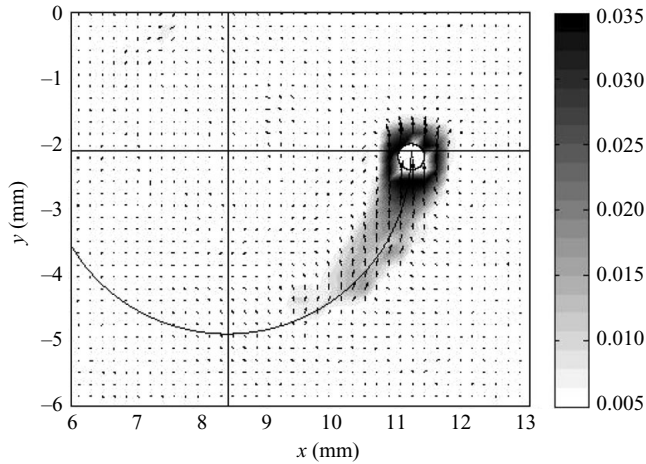


FIGURE 4. A small size bubble ( $d \approx 0.4$  mm,  $Re \approx 20$ ,  $Ro \approx 7$ ) and its perturbation area. The perturbed velocity field is obtained by high-speed PIV. The bubble is represented by the white circle. The axis of rotation of the tank lies at the intersection of the black horizontal and vertical axes. The circular line is what the streamline of the flow would be at equilibrium distance  $r_e$  without the bubble. The velocity perturbations induced by the bubble are represented by the vectors and their magnitude by the greyscale. The white zone close to the bubble corresponds to an area in which there were not enough seeding particles to have correct velocity vectors. For such small bubbles the perturbed zone is very restricted. The incoming flow on the bubble does not feel the perturbation whatever the equilibrium position is.

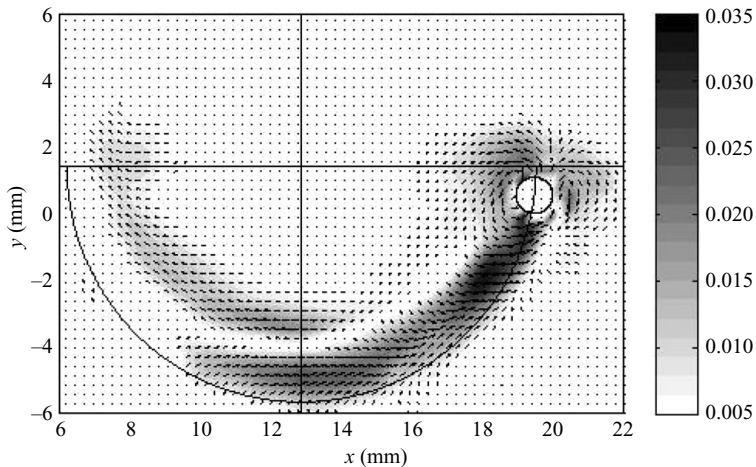


FIGURE 5. Same as in figure 4 but for a medium size bubble ( $d \approx 1.1$  mm,  $Re \approx 130$ ,  $Ro \approx 7$ ). In this configuration, the perturbed zone extends farther downstream from the bubble and its lateral expansion is significantly wider. But as shown here, it does not affect the incoming flow. The wake appears to be more curved than the streamlines of the undisturbed flow.

is comparatively wider. When the equilibrium position is far enough from the centre of the tank ( $6-7 \lesssim Ro$ ), the wake vanishes over a distance of the order of  $\pi r_e$ , and so does not perturb the incoming flow on the bubble (see figure 5). As can also be seen in the figure, a curvature of the wake greater than that of the streamlines of the undisturbed flow is frequently observed. The fact that the wake bends inwards is



FIGURE 6. Long-time exposure for a large bubble ( $Re > 100$ ).  $Ro < 6$ . Strong coupling between the bubble, the flow and two co-rotating vortex occurs with a  $2\omega$  frequency. This frequency can be seen as the signature of that coupling, so, no forces are measured when it appears in the spectrum of the bubble locations around equilibrium.

linked to an inward flow developing at the outer edge of the wake and visible at the bottom of the figure. The reasons for this inflow are still unclear. When  $Ro \leq 6-7$  a precession of the bubble occurs and a peak appears in the power spectrum of the displacements of the bubble ( $x$ -position of the bubble for instance), at the frequency  $2\omega$  (see figure 7*b*). This peak is absent when the precession does not take place (see figure 7*a*). As will be seen in what follows this precession strongly affects the incoming flow on the bubble, which is then no longer an *SBRH*. Forces are not measured in this configuration. In the geostrophic limit where  $Ro \ll 1$ ,  $R_\omega \gg 1$  we know (Batchelor 1967) that the mass of fluid displaced by any object (bubble or solid particle) is subject to the Coriolis force, which in turn induces an opposite force on the object, expressed as

$$\mathbf{F} = 2(\rho_l V_b)\boldsymbol{\omega} \times \mathbf{U}. \quad (3.1)$$

Under the action of this force, the object describes a uniform circular motion at frequency  $2\omega$ . A two-way coupling then develops between the object and the fluid, the fluid around the object being affected by this motion. In the present case,  $R_\omega$  is of the order of magnitude of 10–30 and  $Ro$  is approaching 1 ( $Ro \leq 6-7$ ), thus the above reasoning cannot be strictly applied. But there are strong reasons to think that the observed precession with a  $2\omega$ -peak in the spectrum is a reminiscence of this rigorous circular motion. As can be seen in figure 6, the precession of the bubble is coupled with the release of two co-rotating vortex behind the bubble, that come periodically towards the rotation axis of the flow. This coupling perturbs even the flow towards the rotation axis as well as the incoming flow on the bubble. As mentioned before, in this context the incoming flow on the bubble is no longer an *SBRH*.

### 3.3. Bubble's equilibrium – force measurements

With the exception made of the experiments of §4.2.2, all force measurements were made in demineralized water, without adding any seeding particles. To visualize the bubble, the tank is lit up from behind by a white spotlight. The camera looks into the tank from the front face. The alignment between the camera and the tank was adjusted at best. The remaining small deviations were quantified. They are taken into account for the calculation of the equilibrium position of the bubble. For each run a series of around 2200 images of the bubble at equilibrium are recorded. Then, image



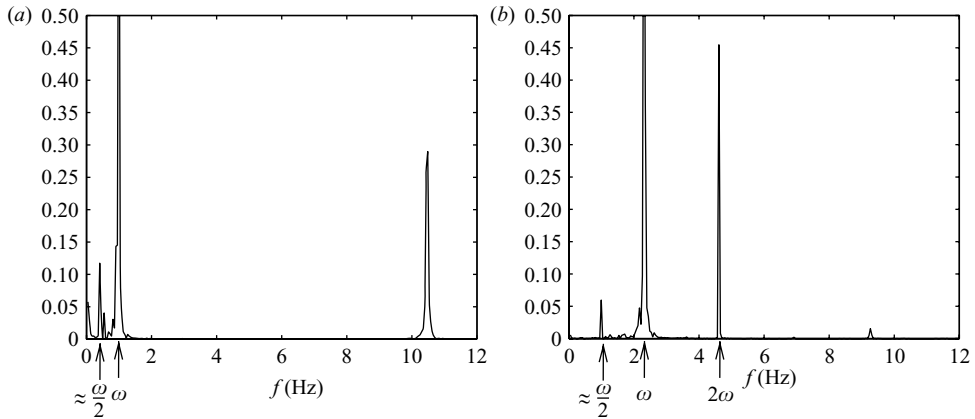


FIGURE 7. Example of typical power spectrum of the  $x$  position of the bubble. (a) Large bubbles ( $d \geq 1$  mm) far from the axis ( $Ro \geq 10$ ); peaks: approx.  $\omega/2$ ,  $\omega$ , approx. 10 Hz and (b) bubble close to the axis; peaks: approx.  $\omega/2$ ,  $\omega$ ,  $2\omega$ .

treatment is used to determine, for each image, the size of the bubble, its aspect ratio and its equilibrium position. The whole procedure is fully described in Rastello *et al.* (2007). For each image, the dimensionless numbers and coefficients are worked out. For each of them the mean over the whole set gives the value for the run. It must be mentioned that the bubble never stabilizes completely onto its equilibrium position, even after a very long wait. Small movements remain. Their magnitude is of the order of the tenth of a millimetre. They induce oscillations of the dimensionless numbers and coefficients. These oscillations are small and do not prevent determination of the mean values. The frequencies that appear in these bubbles' small motions show interesting features. Indeed, when looking at the power spectrum of the displacements ( $x$  position for instance) (see figure 7), one can notice that noise is nearly non-existent. Well peaked recognizable isolated peaks appear. One corresponds to the  $\omega$ -rotation rate of the tank and is present in all experiments. A second one at a frequency close to  $\omega/2$  is also very often observed, but its origin could not be determined. Two additional peaks are identified for certain flow situations. As mentioned before, a  $2\omega$  peak appears when the bubble is too close to the rotation axis (figure 7b). This observation has been used to remove from the database the experiments in which force measurements cannot be made. Finally, for large bubbles ( $Re \geq 150$ ) with an equilibrium position far from the axis of rotation of the flow ( $Ro \geq 10$ ), a peak appears around 10 Hz (see figure 7a). There are serious reasons to think that this frequency is a signature of the vortex shedding in the wake behind the bubble and of the coupled oscillating motion it causes on the bubble. Indeed, when looking at the vorticity in the wake behind the bubble, vorticity releases are observed with a frequency of the order of 10 Hz (see figure 8). The existence of these vorticity releases over that particular range of Reynolds numbers and at that frequency is consistent with results in the literature. The onset of wake instability, like the frequency of vortex shedding, strongly depends on bubble size, shape, degree of contamination (Leal 1989; Bel Fdhila & Duineveld 1996) and on the type of flow (Sakamoto & Haniu 1995). For contaminated bubbles behaving like solid spheres, the critical Reynolds numbers where wake instability and vortex shedding is expected to set in is  $Re_c \approx 175$  according to numerical simulations (Kim & Pearlstein 1990) and  $Re_c \approx 202$  according to experiments (Hartunian & Sears 1957; Bel Fdhila & Duineveld 1996). This corresponds to the upper range

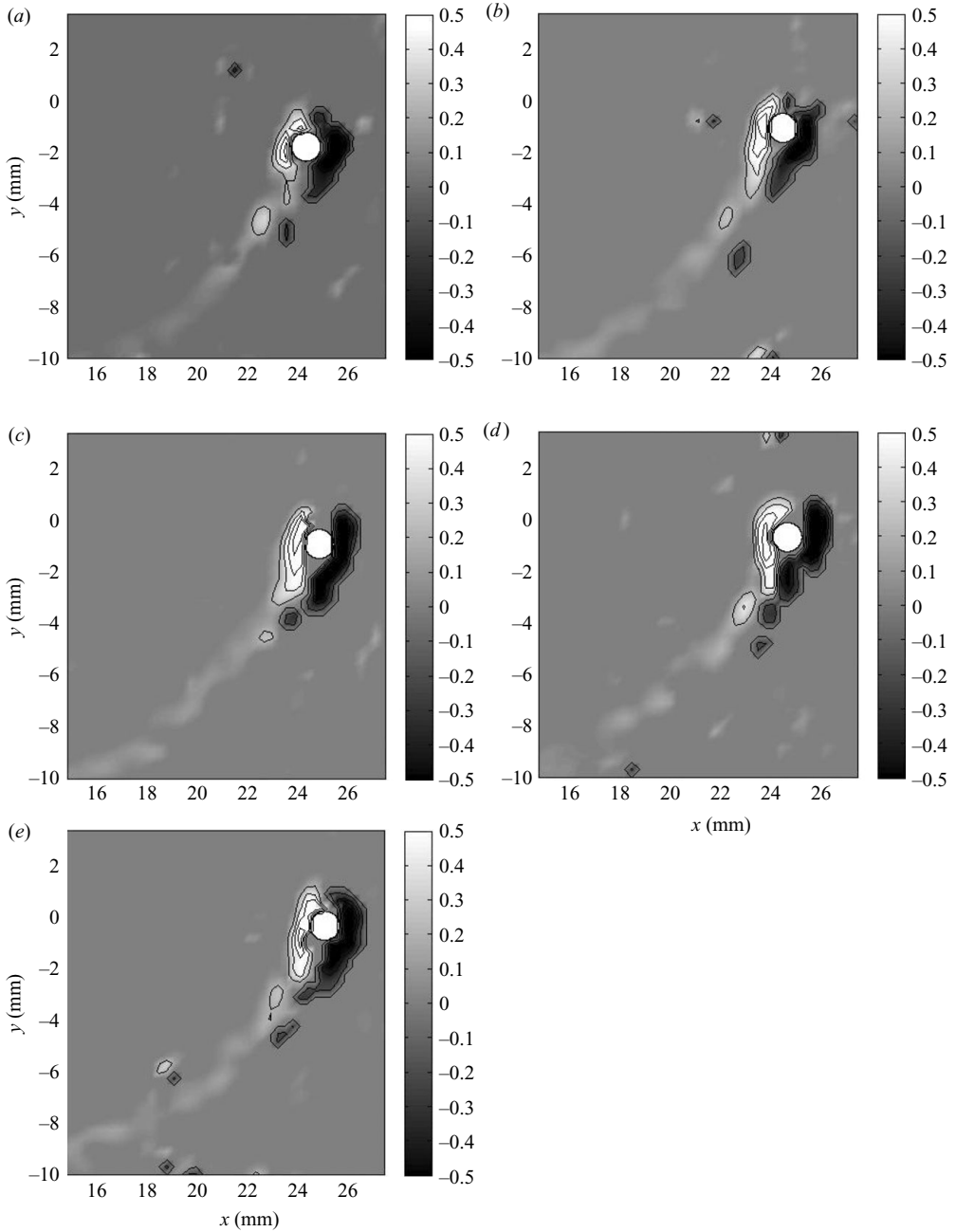


FIGURE 8. Maps presenting the bubble ( $d \approx 1.2$  mm,  $Re \approx 150$ ) and the vorticity at different times. (a)  $t = t_0$ , (b)  $t = t_0 + 1/10$  s, (c)  $t = t_0 + 2/10$  s, (d)  $t = t_0 + 3/10$  s and (e)  $t = t_0 + 4/10$  s. Vorticity releases are observed behind the bubble, with a frequency of approximately 10 Hz.

investigated here. The typical frequencies reported in these studies vary between 8 Hz and 11 Hz depending on bubble size, which is not far from our observations. In other experiments where bubbles can be considered as rising in pure liquid (Lunde & Perkins 1998; de Vries *et al.* 2002), the frequency of vortex shedding measured

---

	$Re$ (%)	$Ro$ (%)	$C_D$ (%)	$C_L$ (%)
$Re \geq 50$	5	5	15	10
$Re < 50$	10	10	20	100

---

TABLE 1. Order of magnitude of the uncertainties estimated with the standard propagation method for the different parameters and for two different Reynolds ranges.

---

$\sigma_{Re}$	$\sigma_{Ro}$	$\sigma_{C_D}$	$\sigma_{C_L}$
0.38	0.16	0.017	0.025
1.22	0.31	0.077	0.115

---

TABLE 2. Statistical uncertainties. Mean standard deviation for the different parameters (first row: filtered dataset, second row: non-filtered dataset).

for instance by Lunde & Perkins (1998) is of the order of 12 Hz. This remains within the same order of magnitude as our value, although the mechanism of vortex accumulation and wake dynamics strongly differ in that case. A small oscillation of the bubble in the direction parallel to the axis of rotation is also sometimes observed, but it was not possible to measure these small movements with the present measuring device. While determining the dimensionless numbers and coefficients, uncertainties were estimated in two complementary ways. For each quantity ( $Re$ ,  $Ro$ ,  $C_D$ ,  $C_L$ ), the uncertainties were first calculated by adding the uncertainties of each parameter they were function of, according to the standard propagation method (table 1). However, one may ask the degree of relevancy of the uncertainties thus estimated. In particular the uncertainty on  $C_L$ , is of the order of 100 % for  $Re < 50$ . This seems excessive in view of the limited dispersion reported in figure 12 over that range. This arises from the fact that  $\theta_e$ , which is the main contributor to the overall uncertainty in  $C_L$ , is very close to 0 in this case (the equilibrium point is very close to the horizontal axis). A statistical uncertainty for each quantity was therefore calculated in a second step. The procedure is as follows. For each run, the spectrum of the quantity is computed and the peaks due to the oscillations of the bubble are removed ( $\omega$  and  $\omega/2$ ). Then the histogram of this filtered quantity is plotted. It appears to be well fitted by a Gaussian function, showing that each filtered dataset follows a normal distribution. Finally the standard deviation for each fit is calculated and an average  $\sigma$  over all the runs is made. This average value presented in table 2 is justified by the fact that the standard deviation does not vary significantly over the range covered by each quantity. The statistical dispersion is at most  $\pm 2\sigma$  within a 95.5 % confidence interval and remains weak. The mean standard deviation of the non-filtered data is also reported in the same table. Comparison between the two shows how bubbles' oscillations contribute to the overall dispersion of our measurements.

## 4. Forces on the bubble

### 4.1. Drag force

The first step was to test the purity of the demineralized water. This was done by determining the drag coefficient for rising bubbles in the tank at rest. By comparing the present data with existing ones for clean bubbles on the one hand and for solid particles on the other hand, we can estimate the importance of the contamination

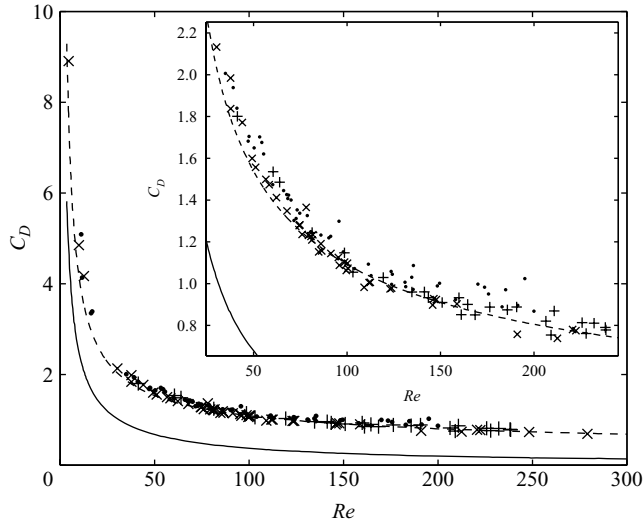


FIGURE 9. Drag force versus Reynolds number. The inserted figure is a zoom of a part of the principal one. —: clean bubble in a uniform flow (Clift *et al.* 1978), - - -: solid sphere in a uniform flow (Mei, Klausner & Lawrence 1994), +: rising bubbles in the tank at rest, ●: bubbles in the *SBRH* with  $Ro < 10$ , ×: bubbles in the *SBRH* with  $Ro \geq 10$ . The fluid is for all these experiments not seeded demineralized water.

of bubble interfaces in our fluid. Indeed depending on the amount of contaminants on their interface, bubbles have a behaviour somewhere in between that of clean bubbles and solid particles. The points of the present study fall on the curve that describes solid spheres (see figure 9). This shows that the demineralized water we use cannot be treated as a pure liquid with our operating conditions. The interface of the bubbles is thus contaminated. This result is not really surprising. We do not use a Millipore purification system as in Duineveld (1995) or de Vries *et al.* (2002). It is then difficult with our experimental procedure to keep the facility extremely clean. Finally, bubbles are very small, so their interfaces are contaminated more easily and rapidly than larger ones (Bel Fdhila & Duineveld 1996; Cuenot, Magnaudet & Spennato 1997; Alves *et al.* 2005). Since the data fall on the curve that describes solid spheres, bubbles are typically in the regime where their interfaces are highly contaminated and the terminal velocity is independent of the contaminants concentration (Clift *et al.* 1978). Referring to Bel Fdhila & Duineveld (1996) and Cuenot *et al.* (1997), this occurs when nearly the rear half of the bubble surface is covered by surfactants, and the shear stress and the pressure are dramatically increased at the leading edge of the spherical cap-angle thus formed. This is the regime commonly encountered over that range of diameters in applications involving water, which is an argument to think that the results of the study will apply to a number of practical situations. The second step was to measure the drag of the bubble in the *SBRH*. On the same figure as before the results for the bubble in the *SBRH* are plotted. A small but non-negligible effect of the rotation of the fluid can be noticed. Indeed, when the fluid is rotating, the values of  $C_D$  for the bubbles have a tendency to be above the curve for solid spheres in a uniform flow. The gap with the curve appears to increase when  $Ro$  decreases. An increase of the same order of magnitude has already been noticed by van Nierop *et al.* (2007). Legendre & Magnaudet (1998) have studied the increase of the drag with the shear for a bubble in a linear shear flow. They proposed

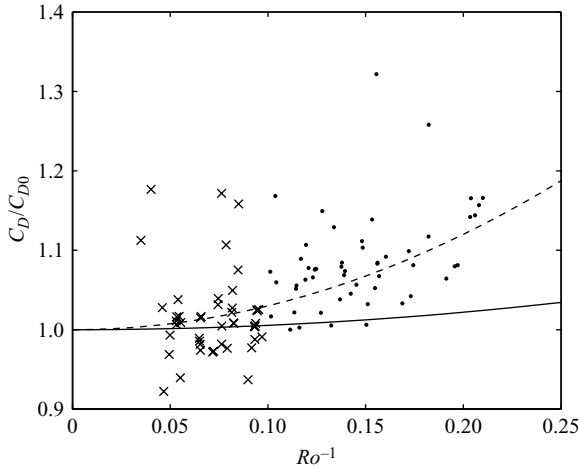


FIGURE 10.  $C_D/C_{D0}$  as a function of  $Ro^{-1}$ . —:  $1 + 0.55Ro^{-2}$  (Legendre & Magnaudet 1998), - - -:  $1 + 3Ro^{-2}$ , ●: bubbles in the SBRH with  $Ro < 10$ , ×: bubbles in the SBRH with  $Ro \geq 10$ .

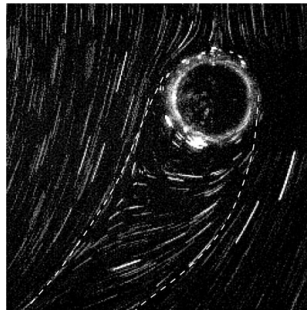


FIGURE 11. Visualization of a bubble and its wake. The visually estimated edges of the wake have been materialized with a dashed line.  $d_b \approx 1$  mm,  $Re \approx 120$ ,  $Ro \approx 8$ ,  $\Omega_b/\omega \approx 1.4$ . The near wake appears to be quite large. This must have an impact on the drag, increasing it.

the following correction for the drag:

$$C_D = C_{D0} \times (1 + 0.55S^2) \quad (4.1)$$

with  $C_{D0}$  the drag coefficient for a bubble in a uniform flow. In their study, van Nierop *et al.* (2007) graphically corrected their drag coefficient with the law of Legendre & Magnaudet (1998). It seems to be enough qualitatively to reduce the gap with the curve for solid particles. Unfortunately no quantitative results are given to which we could compare our results. In the present case the influence of  $S = Ro^{-1}$  appears to be stronger than that found for linear shear flows. Indeed, if one wants to fit the data with a second-order polynomial, the prefactor before  $Ro^{-2}$  is more likely to be 3 than 0.55 (see figure 10). Three differences with Legendre and Magnaudet's study can be pointed out. In a linear shear context, the increase of  $S$  is only linked to an increase of the shear. In the present case, when  $Ro^{-1} = S$  increases, both the shear and the curvature of the streamlines go up. This may have an effect on the drag. A second point is that the present dirty bubble rotates on itself (see §4.2.2 for more details). Indeed, because the bubble's interface is polluted, the no-shear condition at the interface does not hold anymore. Hence, the asymmetry of the flow

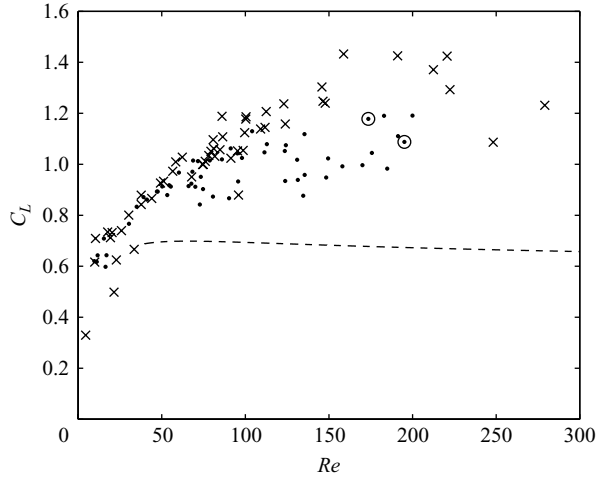


FIGURE 12. Lift force versus Reynolds number. - - - (4.3): fixed clean bubble in a solid body rotating flow (Magnaudet & Legendre 1998). ●: bubbles in the *SBRH* of demineralized water only with  $Ro < 10$ , ×: bubbles in the *SBRH* of demineralized water only with  $Ro \geq 10$ , ⊙: bubbles in the *SBRH* with  $Ro < 10$ , the fluid is the one used to visualize bubble's spinning (demineralized water + seeding particles).

makes the contaminated surface of the bubble rotate. This is probably also a source of increase for the drag force. This hypothesis can be reinforced by the fact that Bagchi & Balachandar (2002a) observed an increase of the drag when the particles they studied were spinning. The last point is surely linked to the two previous ones. While making observations of the bubble and its wake (for more details see §4.2.2) we noticed that the near wake of the bubble in the present *SBRH* conditions is quite wide (see figure 11). This is caused by the non-symmetrical deflection of the flow which is particularly strong in this region. Referring to Magnaudet & Legendre (1998) this deflection is more accentuated than in a linear shear flow for the same  $Re$  conditions, and it seems reasonable to think that this also increases the drag. An important point must be mentioned here. During the phase of visualization of the flow (long-time exposure) it was checked that no Taylor column develops on the front and backsides of the bubble. This was visualized by translating the laser sheet to explore these regions of the flow. This is consistent with the fact that the bubble is on an equilibrium position and that the  $Ro$  number is no lower than 1. The increase of  $C_D$  cannot be assigned to this effect.

#### 4.2. Lift force

##### 4.2.1. Presentation of the results

Figure 12 shows the lift coefficients measured in our *SBRH*, as a function of  $Re$  for different ranges of  $Ro$ . The empirical expression of the lift coefficient for a fixed clean bubble in a rotating flow obtained by Magnaudet & Legendre (1998) from their numerical simulations (4.3) is plotted on the same figure. Several remarks can be made. Firstly, different behaviour is observed below and above  $Re = 60-70$ . Below this value the lift coefficient seems to be independent of the Rossby number. Above, significant dependence can be noticed.  $C_L$  appears to increase when  $Ro$  increases. Secondly, there is an important discrepancy between our data and the empirical expression of Magnaudet & Legendre (1998). The measured lift coefficients are much higher than those of the simulations and do not tend asymptotically like simulations

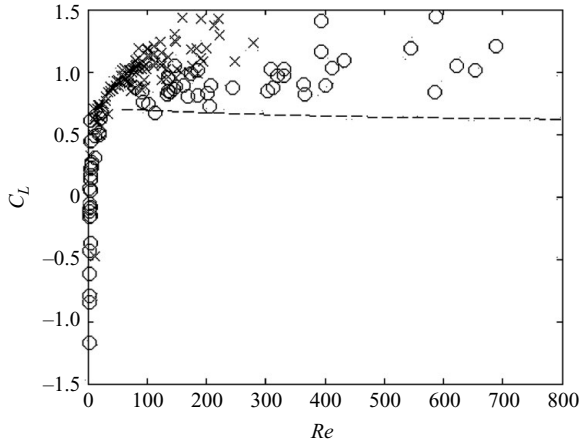


FIGURE 13. Lift force versus Reynolds number. - - -: (4.3): fixed clean bubble in a solid body rotating flow (Magnaudet & Legendre 1998).  $\times$ : results from the present study,  $\circ$ : results from van Nierop *et al.* (2007)'s study.

do, to the 0.5 value of Auton (1987)'s inviscid theory at high Reynolds numbers. Here, although the Reynolds numbers investigated remain smaller than 300, the coefficient seems to tend to 1–1.2, which is more than twice the magnitude obtained by these authors. Comparing the present results with van Nierop *et al.* (2007)'s study brings out some interesting features (see figure 13). For low  $Re$  number values, the results of both studies fall along a same single curve, even if the fluids used are different (water versus glycerine–water mixture). The asymptotic value of  $C_L$  at large Reynolds numbers is approximately 1 in both cases, rather than 0.5. There are other studies that show that for contaminated microscopic bubbles in a vortex (Sridhar & Katz 1995) or solid spheres in an *SBRH* (Bagchi & Balachandar 2002a), lift coefficients are higher than those expected for clean bubbles from the inviscid theory. Here, the interface of our bubbles was proved to be contaminated and it is probable that a boundary condition more like the non-slip type might replace the shear-free boundary condition. This would explain the discrepancy between these simulations and our experiments. The aim of the work presented in the next two parts was to investigate this point in detail by imaging the interface of the bubble.

#### 4.2.2. Bubble's spinning

The interface of the bubble was visualized using a PIV-like method and the high-speed camera with a magnification system (extend tubes). The field of view is typically  $12 \times 10$  mm. The fluid is seeded with very small fluorescent polymer particles (size =  $3 \mu\text{m}$ , density =  $1.05 \text{ g cm}^{-3}$ ). They are illuminated with a laser sheet. The camera takes the images at  $200 \text{ frames s}^{-1}$ . Some of the particles come and cling to the interface of the bubble. Looking at them gives information on the movements of the bubble's interface. As can be observed in figure 14, the bubble's interface is clearly rotating. To avoid any ambiguity, it is useful to specify what this so-called rotation actually describes. What is observed is that some particles rotate around the bubble. Unfortunately, the spatial resolution accessible from the visualizations does not allow us to say whether these particles are at the interface or very near it. Whatever the answer, it is reasonable to think that they rotate with the same velocity as that of the fluid at the interface, as imposed by the boundary conditions

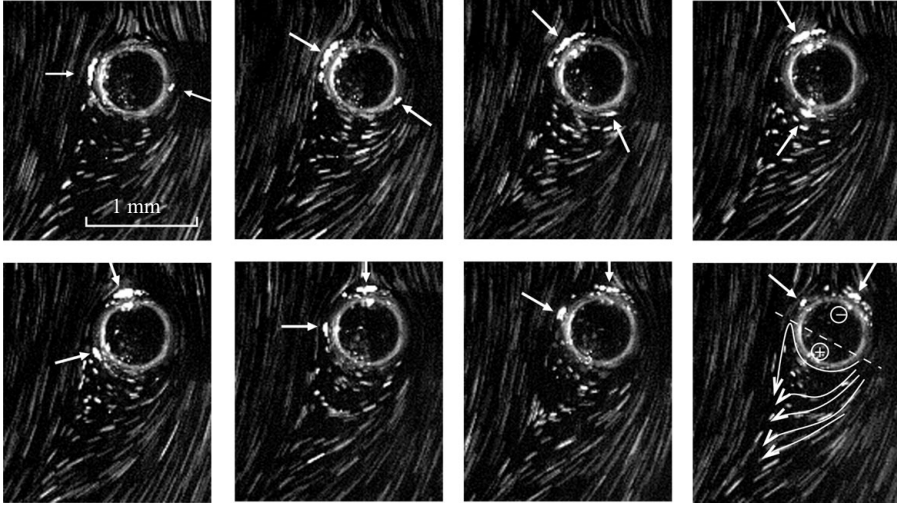


FIGURE 14. Visualization of the rotation of the bubble's interface. The time interval between two images is 20 ms,  $d_b \approx 0.66$  mm,  $Re \approx 50$ ,  $Ro \approx 8$ ,  $\Omega_b/\omega \approx 1.2$ . The marked arrows are there to help to follow the particles stuck on the interface. On the eighth image, the typical zones of the flow are marked. + corresponds to the zone in which the particles at the interface accelerate. - corresponds to the zone in which the particles at the interface decelerate. An idea of the streamlines in the wake is given. One point to notice is the existence of a zone in which the fluid turns back.

on the contaminated surface of the bubble. Thus, for the sake of simplicity we will assimilate their motion to the rotation of the interface and speak thereafter of a spinning interface. This interface spinning can be viewed as the difference between the circulation of the liquid at the contaminated interface and that which would exist around a clean bubble of the same diameter, with the consequence it implies on the lift force. This rotation occurs for every bubble, whatever its size or equilibrium position. Various specificities of this rotation can be mentioned. The rotation of the interface is not uniform. In the area where the interface is close to the bubble's wake, the particles stuck on the interface accelerate. In the region which is close to the incoming flow, they decelerate. This can be noticed by looking at the evolution of the angular space between arrows on the sequence of images in figure 14. We deduce that these particles are not in a solid body rotation as the surface of a solid sphere would be. Their behaviour at the interface is complex and is something in between the shear-free and non-slip condition. However, a mean rotation rate was computed for each bubble ( $\Omega_b$ ). This was done by counting the number of images necessary for a particle on the interface to make a complete turn. This rotation rate divided by the one of the tank ( $\omega$ ) is plotted in figure 15. From this figure it can be noticed that the rotation rate of the bubble's interface is higher than that of the tank. On the other hand, if one compares the velocity of the interface (in  $\text{ms}^{-1}$ ) to the velocity of the fluid at the centre of the bubble, the ratio is of the order of 0.1–0.2. One consequence of the interface's rotation is the presence of a horizontal component of the fluid velocity in the wake, near the bubble's interface. This ends with the streamline turning back where the wake attaches again (see last image of figure 14). This induces asymmetry in the wake which increases the asymmetry due to the *SBRH*. No significant recirculation is noticed around the top of the bubble's interface. The stagnation point of the incoming flow appears to be right in the middle



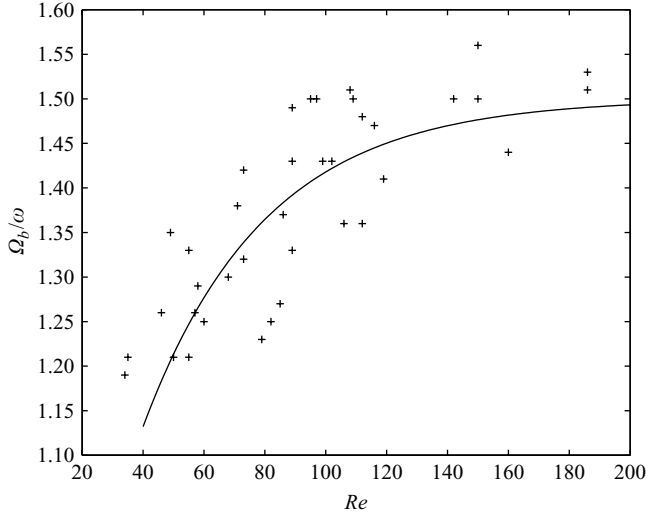


FIGURE 15. +: ratio between the mean rotation rate of the bubble's interface ( $\Omega_b$ ) and the rotation rate of the tank ( $\omega$ ) versus the Reynolds number. —: data fitting:  $1.5 - \exp(-Re/40)$ .

of the interface regarding the incoming flow. No shift was observed. To be sure that the presence of the particles does not modify the characteristics of the bubble, two measurements of the lift forces were taken with the seeding particles in the water. They are represented in figure 12. No difference can be noticed with the values of the lift without particles in water. In addition, while making all the other experiments with seeding particles the bubbles were examined qualitatively from the point of view of the forces. For all the experiments, the equilibrium positions were found to be the same as would have been observed for a bubble in water without seeding particles and with the same other experimental conditions. Hence, it can be considered that neither the particles nor the surfactants used by the manufacturer to avoid their aggregation modify the forces experienced by the bubble.

#### 4.2.3. Magnus and shear lift forces

At this stage the purpose is to see if the combined effect of shear and the Magnus-like effect can explain the lift forces we measured. Bagchi & Balachandar (2002a) did numerical simulations on rotating and non-rotating particles in a linear shear flow. They show that for intermediate Reynolds numbers it is possible to linearly superimpose the effects of shear and of Magnus for the lift

$$C_L(\text{shear, Magnus}) = C_L(\text{shear, 0}) + C_L(0, \text{Magnus}). \quad (4.2)$$

We make the assumption that it is also possible here for the bubbles. We then superimpose the lift force on a bubble only due to the *SBRH* and the lift force due to the Magnus effect for a spherical body in a uniform flow. To our knowledge, no lift force for a non-rotating contaminated bubble in an *SBRH* has yet been computed. Hence, as a first approximation, we use Magnaudet & Legendre (1998)'s expression for the lift force for a clean bubble in an *SBRH*

$$C_L(\text{shear, 0}) = \frac{1}{2}(1 + C_A) - 0.25 + 1.2Re^{-1/3} - 6.5Re^{-1} \quad (4.3)$$

with  $C_A$  given by Lamb (1934)'s expression (see §2). The Magnus contribution is the one proposed by Bagchi & Balachandar (2002a) for a rotating particle in a uniform

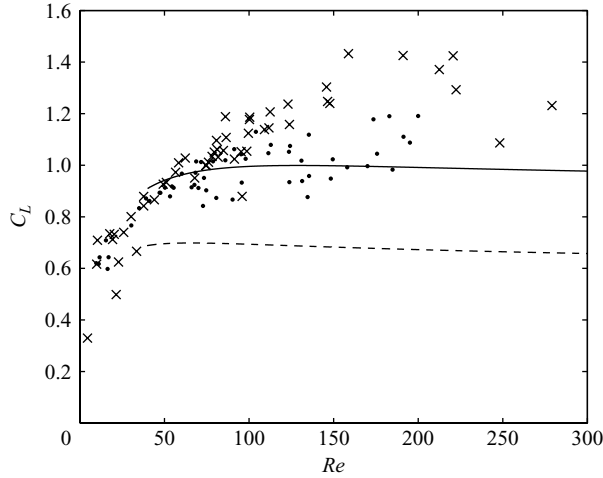


FIGURE 16. Lift force versus Reynolds number. - - -: (4.3): fixed clean bubble in a solid body rotating flow (Magnaudet & Legendre 1998). ●: bubbles in the *SBRH* with  $Ro < 10$ , ×: bubbles in the *SBRH* with  $Ro \geq 10$ , —: superposition of a lift component due to shear and a lift component due to a Magnus effect: (4.6).

flow and applied to the present configuration

$$C_L(0, \text{Magnus}) = 0.55 \frac{\Omega_b d}{\omega r_e} \times \frac{3r_e}{8d}. \quad (4.4)$$

In Bagchi & Balachandar (2002a), the Magnus-like coefficient was defined as follows:

$$F_L(0, \text{Magnus}) = 0.55 \frac{\Omega_b d}{\omega r_e} \times \frac{1}{2} \rho_l S_b U_r^2$$

with  $S_b$  the projected particle area,  $U_r$  its relative velocity. This is why, to be consistent with the notations in this paper, the last factor appears in  $C_L(0, \text{Magnus})$  in (4.4). In the expressions of  $C_L(\text{shear}, 0)$  and of  $C_L(0, \text{Magnus})$ , we use  $Re$  determined experimentally for each bubble.  $\Omega_b/\omega$  is estimated using the experimental fit of the data of §4.2.2:

$$\frac{\Omega_b}{\omega} = 1.5 - \exp\left(-\frac{Re}{40}\right). \quad (4.5)$$

The summation of (4.3) and (4.4) yields a lift coefficient of the form

$$C_L = \frac{1}{2}(1 + C_A) - 0.25 + 1.2Re^{-1/3} - 6.5Re^{-1} + 0.55 \times \frac{3\Omega_b}{8\omega}. \quad (4.6)$$

Equation (4.6) is plotted together with the experimental data in figure 16. The interesting point is that there is now no longer any discrepancy between the curve and experimental data, without any adjusting parameter. To take into account the influence on  $Ro$ , it is probably necessary to take into account also nonlinear effects between both phenomena (shear and Magnus). Indeed, depending on the equilibrium position of the bubble, the wake of the bubble is modified. So is the accelerating and decelerating zones associated with the rotation of the bubble. It is worth noting that Sridhar & Katz (1995) conjectured that the free rotation of the microscopic bubbles in their experiments was possibly responsible for the enhanced lift force in a vortex. Here is some proof that such a rotation actually exists for spherical millimetre bubbles

in an *SBRH* when interfaces are contaminated and that it has a significant effect on the forces.

## 5. Conclusion

The purpose of the present study was to measure the drag and lift forces on a single bubble at equilibrium in a horizontal *SBRH*. Measurements were taken in demineralized water i.e., a contaminated fluid as regards bubble's interfaces. This point was checked by measuring the drag coefficient of bubbles rising in such water when the rotation is stopped. The coefficients were found to follow the curve of solid spheres, indicating that interfaces are actually contaminated. Various tests were then carried out to qualify the flow. Firstly, the flow without any bubble was characterized as actually being an *SBRH*. Secondly, the flow induced by the bubble's presence was studied. For small diameter bubbles ( $Re \leq 60-70$ ), or large diameter bubbles which stabilize at a distance greater than 6–7 diameters from the centre of the flow ( $Re \leq 60-70$ ), the wake decays in less than half a turn, and so does not affect the incident flow on the bubble. The flow field can be considered in a state of *SBRH*. Now, if the equilibrium position of large bubbles is less than 6–7 diameters from the centre of the flow ( $Ro < 6-7$ ), the incident flow on the bubble is affected. Strong two-way coupling develops between the bubble-induced flow, the centre of the *SBRH* and the bubble, with a frequency equal to twice the angular frequency of rotation of the tank. This provides a criterion that was used to remove the force measurements obtained in such situations. The lift and drag forces on the bubble were determined by measuring the equilibrium position of the bubble from images of the flow. With the tank rotating, the drag coefficients lie above the curve for solid spheres and significantly increase when  $Ro$  decreases. This increase is larger than that expected for example from the numerical simulations of Legendre & Magnaudet (1998) on a clean bubble fixed in a linear shear flow. The reasons for this have not yet been completely understood, but we can suspect that these differences arise from a higher non-symmetry of the flow and the particular boundary condition at the interface of the bubble. Indeed, the curvature of the streamline and the spinning of the bubble, which is one of the important findings of this paper, accentuate the non-symmetry of the wake near the rear of the bubble and doing so probably increases the drag. The lift coefficients are found to depend on  $Ro$  for  $Re > 60-70$  and to be insensible to it below. They increase when  $Ro$  increases, unlike the drag coefficients which decrease. Their magnitudes are approximately twice as high as the simulations of Magnaudet & Legendre (1998) for a clean bubble and do not tend asymptotically, as simulations do, to the value 0.5 of Auton (1987)'s potential theory at high Reynolds numbers. The origin of these higher magnitudes have been determined by visualizing in detail the interface of the bubble. A careful study of this interface showed that it is spinning. The rotation rate  $\Omega_b/\omega$  was quantified. It was found to be higher than 1 and to increase with the Reynolds number. A simple model for the lift coefficient has been proposed combining the effect of shear and the effect of this spinning of the bubble. The predictive curve obtained with this model agrees rather well with the data, without any adjusting parameter.

Thanks to E. Loth for his interesting comments on drag results and to B. Pier and A. Biesheuvel for many fruitful discussions and remarks. The authors would also like to thank M. Michard for his useful suggestions concerning vorticity determination by PIV, and N. Quennouz for some post-treatment of the results.

## REFERENCES

- ALVES, S. S., ORVALHO, S. P. & VASCONCELOS, J. M. T. 2005 Effect of bubble contamination on rise velocity and mass transfer. *Chem. Engng Sci.*, **60**, 1–9.
- AUTON, T. R. 1987 The lift force on a spherical body in a rotational flow. *J. Fluid Mech.* **183**, 199–218.
- BAGCHI, P. & BALACHANDAR, S. 2002a Effect of free rotation on the motion of a solid sphere in linear shear flow at moderate re. *Phys. Fluids* **14** (8), 2719–2737.
- BAGCHI, P. & BALACHANDAR, S. 2002b Shear versus vortex-induced lift force on a rigid sphere at moderate re. *J. Fluid Mech.* **473**, 379–388.
- BATCHELOR, G. K. 1967 *An introduction to fluid dynamics*. Cambridge University Press.
- BEL FADHILA, R. & DUINEVELD, P. C. 1996 The effect of surfactant on the rise of a spherical bubble at high Reynolds and Peclet numbers. *Phys. Fluids* **8**, 310–321.
- CANDELIER, F., ANGILELLA, J.-R. & SOUHAR, M. On the effect of the Boussinesq-Basset force on the radial migration of a stokes particle in a vortex. *Phys. Fluids* **16** (5), 1765–1776.
- CLIFT, R., GRACE, J. R. & WEBER, M. E. *Bubbles, Drops and Particles*. Academic Press.
- CUENOT, B., MAGNAUDET, J. & SPENNATO, B. 1997 The effects of slightly soluble surfactants on the flow around a spherical bubble. *J. Fluid Mech.* **339**, 25–53.
- DUINEVELD, P. C. 1995 The rise velocity and shape of bubbles in pure water at high Reynolds number. *J. Fluid Mech.* **292**, 325–332.
- HARTUNIAN, R. A. & SEARS, W. R. 1957 On the instability of small gas bubbles moving uniformly in various liquids. *J. Fluid Mech.* **3**, 27–47.
- JUANEDA, Y. & COLIN, C. 9–13 July 2007 Bubble dynamics in a cylindrical Couette flow. In *Sixth International Conference on Multiphase Flows*, Leipzig.
- KIM, I. & PEARLSTEIN, A. J. 1990 Stability of the flow past a sphere. *J. Fluid Mech.* **211**, 73–93.
- LAMB, H. 1934 *Hydrodynamics*, 6th edn. Dover.
- LEAL, L. G. 1989 Vorticity transport and wake structure for bluff bodies at finite Reynolds number. *Phys. Fluids* **1**, 124–131.
- LEGENBRE, D. & MAGNAUDET, J. 1997 A note on the lift force on a spherical bubble or drop in a low-Reynolds-number shear flow. *Phys. Fluids* **9** (11), 3572–3574.
- LEGENBRE, D. & MAGNAUDET, J. The lift force on a spherical bubble in a viscous linear shear flow. *J. Fluid Mech.* **368**, 81–126.
- LUNDE, K. & PERKINS, R. J. 1998 Shape oscillations of rising bubbles. *Appl. Sci. Res.* **58**, 387–408.
- MAGNAUDET, J. & EAMES, I. 2000 Dynamics of high re bubbles in inhomogeneous flows. *Annu. Rev. Fluid Mech.* **32**, 659–708.
- MAGNAUDET, J. & LEGENBRE, D. 1998 Some aspects of the lift force on a spherical bubble. *Appl. Sci. Res.* **58**, 441–461.
- MEI, R., KLAUSNER, J. & LAWRENCE, C. 1994 A note on the history force on a spherical bubble at finite Reynolds number. *Phys. Fluids* **6**, 418–420.
- VAN NIEROP, E. A., LUTHER, S., BLUEMINK, J. J., MAGNAUDET, J., PROSPERETTI, A. & LOHSE, D. 2007 Drag and lift forces on bubbles in a rotating flow. *J. Fluid Mech.* **571**, 439–454.
- NACIRI, A. 1992 Contribution à l'étude des forces exercées par un liquide sur une bulle de gaz: portance, masse ajoutée et interactions hydrodynamiques. PhD thesis, Ecole Centrale de Lyon.
- RASTELLO, M., MARIÉ, J.-L., GROSJEAN, N. & LANCE, M. 9–13 July 2007 Study of bubble's equilibrium in a rotating flow. In *Sixth International Conference on Multiphase Flows*, Leipzig.
- SAFFMAN, P. G. 1965 The lift force on a small sphere in a slow shear flow. *J. Fluid Mech.* **22**, 385–400. Corrigendum: *J. Fluid Mech.*, **31**, 624 (1968).
- SAKAMOTO, H. & HANIU, H. 1995 The formation mechanism and shedding frequency of vortices from a sphere in uniform shear flow. *J. Fluid Mech.* **287**, 151–171.
- SRIDHAR, G. & KATZ, J. 1995 Drag and lift forces on microscopic bubbles entrained by a vortex. *Phys. Fluids* **7** (2):389–399.
- DE VRIES, A. W. G., BIESHEUVEL, A. & VAN WIJNGAARDEN, L. 2002 Notes on the path and wake of a gas bubble rising in pure water. *Intl J. Multiphase Flow* **28**, 1823–1835.